Broadband, High-Frequency Permittivity Characterization for Epitaxial $Ba_{1-x}Sr_xTiO_3$ Composition-Spread Thin Films

Eric J. Marksz,[1,2] Aaron M. Hagerstrom,[2] Xiaohang Zhang,[1] Naila Al Hasan,[1] Justin Pearson,[1] Jasper A. Drisko,[2] James C. Booth,[2] Christian J. Long,[2] Ichiro Takeuchi,[1] and Nathan D. Orloff*[,2]

[1] *Department of Materials Science and Engineering, University of Maryland, College Park, Maryland 20740, USA*

[2] *National Institute of Standards and Technology, RF Electronics Group, RF Technology Division, Communications Technology Laboratory, Boulder, Colorado 80305, USA*

(Received 25 October 2020; accepted 16 April 2021; published 24 June 2021)

Next-generation millimeter-wave (> 30 GHz) telecommunications electronics must be compact, energy efficient, and have good thermal management. Tunable materials may play a role in meeting these requirements for millimeter-wave front-end devices, but there are few models or even measurements of tunable dielectrics at these frequencies. Here, we report on the adaptation and development of high-frequency dielectric spectroscopy techniques for composition-spread thin films from 100 MHz to 110 GHz. Our comprehensive technique sequentially probes the composition, frequency, and electric field dependence of the complex permittivity in a combinatorial thin film library, which provides a platform to rapidly explore functional materials for emerging telecommunications electronics. This is achieved by modifying existing on-wafer transmission line permittivity measurement techniques to obtain a compact set of test devices that can be patterned to extract the complex permittivity in multiple regions of a thin film. We demonstrate this technique by applying it to composition-spread $Ba_{1-x}Sr_xTiO_3$ thin films spanning compositions from $x = 0$ to $x = 1$. The systematic approach to materials growth inherent in combinatorial synthesis allows for a comprehensive picture of the $Ba_{1-x}Sr_xTiO_3$ system. Our continuous, quantitative measurements provide an encompassing view of the composition- and voltage-dependent trends in the room temperature dielectric properties at millimeter-wave frequencies—from strong, few-picosecond relaxations to no relaxation, and from large relative tunability (n_r > 50% at 75 kV cm^{-1}) to zero tunability. Our work underscores both the utility of our technique, and the need to discover lower-loss, highly tunable electronic materials for next-generation telecommunications.

DOI: 10.1103/PhysRevApplied.15.064061

I. INTRODUCTION

Tunable radio-frequency (rf) front-end devices will likely play a notable role in next-generation microwave and millimeter-wave telecommunications [1,2]. Adaptive devices, such as frequency-agile filters and oscillators, reconfigurable antennas, and tunable phase shifters, present opportunities to reduce cost and boost performance. One method to obtain tunable functionality is to integrate ferroelectric materials into these devices. When compared with competing technologies such as rf micro-electromechanical systems or semiconductor varactor diodes, ferroelectric tunable devices can be more robust, switch faster, and provide higher quality factors [3–5]. While there are many demonstrations of tunable ferroelectric devices at microwave frequencies [6–8], there are few examples at millimeter-wave frequencies above approximately 30 GHz—the frontier for communications.

The ferroelectric materials are themselves a limiting factor, as they should ideally have a low loss tangent for energy efficiency, high thermal conductivity for heat management, and large relative tunability to maximize the tunable bandwidth, among other key requirements [9]. Unfortunately, optimizing these properties in a single material requires compromise. For instance, tunability often comes at the expense of dielectric loss [4]. With ferroelectric materials, one can trade reduced tunability for reduced dielectric loss by operating in the paraelectric state where the operating temperature is greater than the ferroelectric Curie temperature. Operating in the paraelectric state avoids lossy acoustic waves generated by domain-wall and piezoelectric oscillations, but the relative tunability can be an order of magnitude less than it might be in the ferroelectric state [10]. One recent report on strained $Ba_{0.8}Sr_{0.2}TiO_3$ films achieved enhanced performance in the ferroelectric state by taking advantage of resonant domain-wall motion, but the improvement used a narrow-bandwidth resonance in the crystal lattice that

*nathan.orloff@nist.gov

was only prominent at frequencies below 10 GHz [11]. Further discovery of tunable thin films, bolstered by techniques to grow and characterize them more rapidly, will provide an opportunity to develop commercially relevant millimeter-wave tunable ferroelectric devices.

Regardless of the material's state, one prominent source of high-frequency dielectric loss is charged point defects [12–14]. Highly controlled epitaxial growth and careful processing can improve the electrical properties by reducing the number of defects, or their ability to contribute to losses [12,15]. For example, epitaxial Ruddlesden-Popper superlattices accommodate nonstoichiometry by forming planar stacking faults rather than point defects, resulting in some of the best low-loss tunable dielectric properties at millimeter-wave frequencies [16]. While these and other studies improved the tunable dielectric properties, they also highlighted the sensitivity of these materials to composition, structure, and processing. Even typical fluctuations (e.g., chamber temperature or background pressure) in the growth environment during deposition can produce variation in the dielectric properties. This sensitivity is a notable obstacle to developing predictive models and algorithms, because one can convolve effects due to growth and processing with intrinsic response [17]. Controlling growth and processing variables makes screening for higher-performing compounds easier and more reliable.

Combinatorial libraries comprise a multitude of test materials that are grown on a single substrate in a single deposition process [18]. Combinatorial material synthesis provides an opportunity for faster testing of compounds and enables highly consistent growth and processing conditions. High spatial-resolution characterization techniques are then used to measure discrete materials in the library and identify trends in the key material properties of interest. Examples of the application of combinatorial techniques to dielectric thin films for tunable rf devices came in the early 2000s when composition-spread $Ba_{1-x}Sr_xTiO_3$ films were grown on single-crystal substrates via pulsed laser deposition (PLD) and subsequently characterized by scanning evanescent microwave microscopy (SEMM) [19]. The high spatial resolution of SEMM enables measurements of many discrete compositions in a composition-spread thin film, which is a film with a continuous gradient in the chemical composition [20]. Unfortunately, quantitative SEMM measurements at millimeter-wave frequencies are more limited since the calibrations, which are based on lumped-element and image-charge models, are less reliable at these frequencies [21]. While others have proposed approaches to model the SEMM tip-sample interactions for extending this technique to higher frequencies, such high-frequency measurements have not yet been demonstrated [22]. On the other hand, on-wafer transmission line measurements are a readily available, broadband, high-frequency alternative to SEMM, but require several large test devices, which is an obstacle to isolating discrete compositions in a combinatorial library.

Inspired by the advantages of both SEMM and transmission line measurements, this report discusses a modified transmission line technique for characterizing the complex permittivity of combinatorial thin films as a function of composition, applied field, and frequency. We adapt existing coplanar transmission line techniques to create a compact measurement device set that tests discrete compositions on a composition-spread thin film. Our technique takes advantage of well-established calibrations and wide bandwidth spanning from 100 MHz to 110 GHz. We demonstrate our technique by measuring 14 discrete compositions on a single composition-spread thin film of $Ba_{1-x}Sr_xTiO_3$ in which x ranges from $x = 0$ to $x = 1$. Although not as fast as SEMM for combinatorial libraries, our technique is notably faster than characterizing one chip at a time and covers a broad and continuous frequency range. We expect that our fast, comprehensive technique will enable the materials discovery community to gain insight into the relationships between composition, structure, and broadband dielectric properties.

II. METHODS

We use the $Ba_{1-x}Sr_xTiO_3$ system to test our methodology. Over the past two decades, this system has received a great deal of focus owing to its promising tunable dielectric properties. Many reports describe the properties of $Ba_{1-x}Sr_xTiO_3$ under different growth and measurement conditions, including reports on composition-spread $Ba_{1-x}Sr_xTiO_3$ thin films. [15,19]. Since our aim is to improve dielectric property measurement techniques for composition-spread thin films, this rich body of literature provides a general baseline for our expected results. Additionally, the $Ba_{1-x}Sr_xTiO_3$ system displays a stark, easily detected change in the complex permittivity and tunability between $x = 0$ ($BaTiO_3$, BTO) and $x = 1$ ($SrTiO_3$, STO) in our frequency range of interest. Finally, while there have been interesting recent combinatorial studies on heterostructurally alloyed compounds [23], the elegant isostructural nature of the $Ba_{1-x}Sr_xTiO_3$ system simplifies several synthesis and characterization aspects of our study. All that said, this technique could be applied to a wide variety of materials systems.

A. Thin film growth

We grow composition-spread thin films of $Ba_{1-x}Sr_xTiO_3$ via PLD on 10 mm × 10 mm square substrates of (001)-cut $(LaAlO_3)_{0.3}(Sr_2TaAlO_6)_{0.7}$ (LSAT). LSAT ($a = 3.87$ Å) is well lattice matched with both BTO (lattice constant, $a = 4.03$ Å) and STO ($a = 3.91$ Å). Furthermore, LSAT does not contain the twin defects inherent in pure $LaAlO_3$ single crystals that can present surface topography and

hinder optimal device fabrication [24]. Our KrF excimer laser ($\lambda = 248$ nm) pulsed at a rate of 2 Hz and ablated material from a 2.5-cm-diameter sintered ceramic target. The ablated material then condensed on the surface of the LSAT substrate to grow the film.

We generate the composition gradient in the film by alternating between ablation from a pure BTO target and a pure STO target. An automated shadow mask controls the area of the substrate exposed to the plume of ablated material, thereby controlling the spatial distribution of Ba and Sr in the film [Fig. 1(a)]. A program synchronizes the mask movement to the laser pulses ablating the first target (BTO) to grow a "thickness wedge" of BTO [Fig. 1(b)]. Then, the program selects the second target (STO) and performs the opposite process to create an opposing thickness wedge of STO to complete one full layer. Each full layer is approximately 2Å thick, which encourages solutionlike mixing of the Ba and Sr and prevents superlattice formation. The linear composition gradient spans compositions x in $Ba_{1-x}Sr_xTiO_3$ from $x = 0$ to $x = 1$. The gradient region is approximately 7 mm long, leaving a 1.5-mm region of BTO on one side of the gradient, and a 1.5-mm region of STO on the other side. The film is approximately 125 nm thick. The surface temperature of the substrate is maintained at 750 °C, the background oxygen partial pressure is 4 Pa throughout the deposition, and we use an approximate laser energy density of 1.0 J/cm^2.

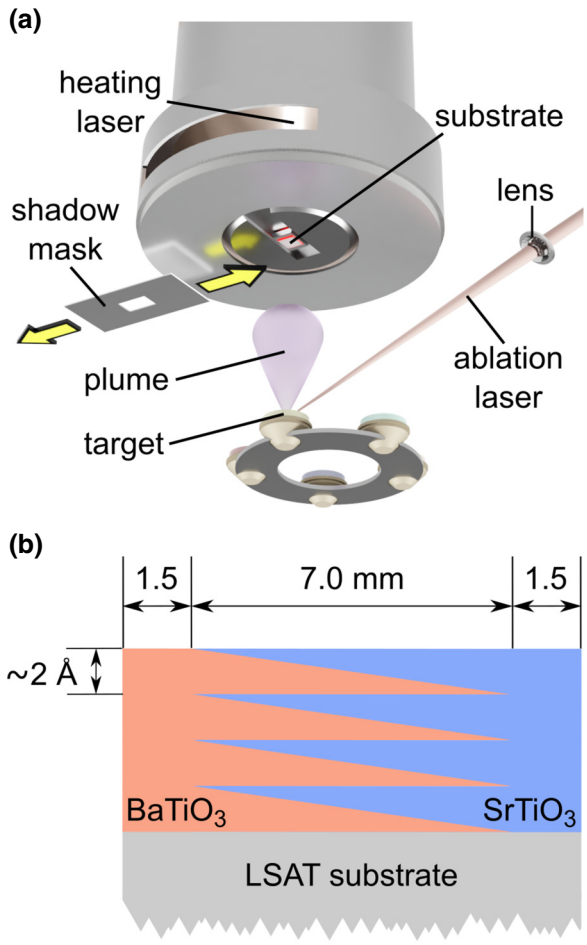

FIG. 1. Combinatorial synthesis techniques enable the growth of composition-spread $Ba_{1-x}Sr_xTiO_3$ thin films. Schematic illustrations of (a) the combinatorial pulsed laser deposition chamber configuration, and (b) the thickness-wedge process to grow a composition-spread thin film from two single-composition targets.

B. Structural and compositional characterization

We initially characterize the structure of the $Ba_{1-x}Sr_xTiO_3$ film with X-ray diffraction (XRD). The XRD system has an automated alignment protocol and a programmable motion stage to scan multiple points along the composition gradient. The diffractometer provides an approximately 1-mm-wide spot of Cu $K\alpha_1$ radiation at the sample surface. Both $\Theta - 2\Theta$ and Φ scans measure the structure of the film and epitaxy relative to the LSAT substrate. Since BTO and STO form the isostructural solid solution $Ba_{1-x}Sr_xTiO_3$, we apply Vegard's law to obtain a rudimentary estimate of the composition gradient profile [25]. While that estimate shows that we produce the desired composition profile, the X-ray spot size is too large to pinpoint the specific compositions x in $Ba_{1-x}Sr_xTiO_3$ where we would perform dielectric properties measurements. Wavelength-dispersive X-ray spectroscopy (WDS) is a high-resolution measurement of the composition profile along the gradient that we use to augment this analysis. We perform our WDS measurements with an electron-probe microanalyzer (EPMA) at an accelerating voltage of 7 kV, which provides an experimentally determined uncertainty on the composition of less than ±3 at. % of the constituent elements.

C. Combinatorial microwave dielectric spectroscopy techniques

Following the structural and compositional characterization, we measure the complex permittivity, $\varepsilon^*(\omega) = \varepsilon'(\omega) + i\varepsilon''(\omega)$, where $\varepsilon'(\omega)$ is the real part of the dielectric permittivity and $\varepsilon''(\omega)$ is the imaginary part of the dielectric permittivity, sometimes referred to as the dielectric loss. We also measure the relative tunability of the combinatorial film. All measurements presented here are performed at 298 K. While a number of lumped-element circuit techniques exist to measure complex permittivity at microwave frequencies [26,27], distributed transmission lines provide more accurate broadband measurements at millimeter-wave frequencies, because of their basis in circuit theory rather than approximations [28]. We begin with coplanar waveguide (CPW) transmission lines [Fig. 2(a)],

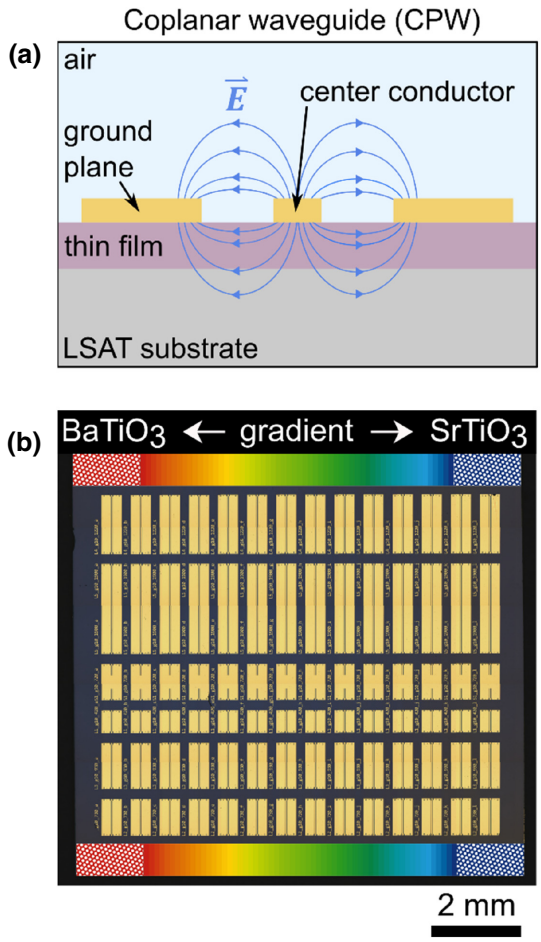

FIG. 2. Coplanar devices patterned on the sample surface enable measurements of thin film dielectric properties. (a) Cross section schematic of a CPW device, illustrating how the electric fields that are generated between the center conductor and ground planes penetrate the thin film and probe the thin film dielectric properties. (b) Top-down optical microscope image of the composition-spread thin film chip with Au CPWs patterned on the surface. Each vertical column of six CPWs is a complete set which samples a single composition x in $Ba_{1-x}Sr_xTiO_3$ from 100 MHz to 110 GHz.

and use their measured scattering (S) parameters in conjunction with the multiline-TRL (Thru-Reflect-Line) technique to determine the propagation constant $\gamma(\omega)$ [29]. The propagation constant is a key quantity that describes the attenuation and phase shift of a rf signal as it is transmitted across the CPW, and it is linked to the dielectric properties of the materials comprising the CPW device. The CPWs are also an ideal device for on-wafer measurements of composition-spread thin films. This is because they can be designed so that the electric fields, which are localized in the gaps between the center conductor and ground planes of the device [30], do not span a large compositional region. In our devices, the 40-μm region comprising the two 10-μm gaps and the 20-μm center conductor of the CPW spans a compositional range of less than 1%, isolating a relatively uniform composition region in the composition-spread film when properly aligned.

The multiline-TRL algorithm also produces accurate estimates for the propagation constant γ from calibrated S parameter measurements of a set of CPWs with varying lengths. The calibrations are required to account for the parasitic electrical effects of the measurement system, such as attenuation and reflection of the test signals in the cables and probes. For the measurements from 100 MHz to 110 GHz described in this work, we use a combination of series resistor [31] and multiline-TRL calibrations [32] with calibration standards fabricated on a custom reference wafer patterned on $LaAlO_3$. To facilitate the use of this technique, all CPWs in each set must have an identical cross section, including identical thin film permittivity. The spatial composition (and permittivity) gradient in our $Ba_{1-x}Sr_xTiO_3$ composition-spread thin film presents an obstacle to a more traditional implementation of this technique [33], which can require large ($>$ 50 mm^2) uniform regions on the thin film. Importantly, the CPW lengths are not arbitrary, and must be optimized to provide an accurate result with reasonable uncertainties across the frequency range of interest.

To adapt this multiline-TRL technique to combinatorial thin film measurements, we optimize our CPW devices such that a full set of six CPW devices for multiline-TRL fit in a single 8-mm-long region. Then we carefully pattern the set perpendicular to the composition gradient [Fig. 2(b)]. The complete pattern includes 14 such sets of devices, allowing us to sample 14 discrete compositions of $Ba_{1-x}Sr_xTiO_3$ spanning the full composition gradient.

We use a maskless aligner tool, which aligns and exposes the desired patterns via a direct-write UV laser instead of a physical mask, and standard lift-off techniques to fabricate the Au test devices [34]. Each device set comprises a short-circuit reflect and five transmission lines of length $l = 0.42,\ 0.73,\ 0.93,\ 1.22,\ 1.90$ mm. The transmission lines consist of a 20-μm-wide center conductor, separated from 200-μm-wide ground planes by 10-μm-wide gaps in which the electric fields are localized as illustrated in Fig. 2(a). The gold conductors are nominally 500 nm thick. We measure the in-plane dimensions and metal thicknesses via optical microscopy and profilometry, respectively, and use these dimensions to construct the finite-element simulations (using ANSYS Q3D) required to extract material properties from the electrical measurements. We use two-dimensional models of the CPWs for these simulations, because these devices have an invariant cross section along their active lengths (i.e., the portion of the device between the probe landing pads). When provided with the measured dimensions of the devices and the material properties of the conductors and dielectric layers, these simulations output values for the distributed circuit characteristics of the devices, which we describe in more detail in the following paragraph. By sweeping

across a range of material properties in these simulations, we obtain a means to map our measurements of the circuit characteristics of the devices to the material properties of the thin films under test. We perform additional WDS characterization after fabrication to verify the alignment of the CPWs to the composition gradient. Compositional variation within all sets of devices is always within the uncertainty achievable by the EPMA, indicating the test pattern is aligned as desired. Along with the composition-spread thin film chip, we also cofabricate (with identical patterning and simultaneous metal deposition) a companion substrate chip made of another single-crystal LSAT substrate from the same batch used for the thin film deposition. The companion substrate serves three critical roles in our analysis: (1) it provides a baseline measurement of the substrate permittivity, (2) it allows us to characterize the properties of the Au conductors, and (3) it provides a tool to validate our finite element method (FEM) simulations.

We make electrical contact with the CPW devices by contacting them with ground-signal-ground probes, and then measure the S parameters from 100 MHz to 110 GHz with a vector network analyzer after performing various standard calibration procedures [29,31,32]. During this process, the chips are placed on a temperature-controlled stage that maintains a temperature of 298 K. Briefly, after measuring and de-embedding the S parameters of the transmission lines, we use the aforementioned multiline-TRL algorithm to generate an estimate of the propagation constant

$$\gamma(\omega) = \sqrt{R(\omega) + i\omega L(\omega)}\,\sqrt{G(\omega) + i\omega C(\omega)}, \quad (1)$$

where $R(\omega)$, $L(\omega)$, $G(\omega)$, and $C(\omega)$ are the frequency-dependent distributed resistance, inductance, conductance, and capacitance, respectively, of the CPW devices. In our experiment, the quantities $R(\omega)$ and $L(\omega)$ are primarily dependent on the CPW geometry and the gold conductor properties, whereas $C(\omega)$ and $G(\omega)$ mostly depend on the CPW geometry and the effective dielectric permittivity $[\varepsilon'(\omega)]$ and dielectric loss $[\varepsilon''(\omega)]$ of the constituent materials, respectively. The LSAT substrate is chosen due to its negligible loss $[G(\omega) \approx 0]$ and constant capacitance in our measured frequency range, which allows us to isolate $R(\omega)$ and $L(\omega)$ from the measured propagation constant of our companion substrate. We use the measured dimensions of the CPW devices to construct our FEM simulations and validate these simulations by comparing the simulated and measured $R(\omega)$ and $L(\omega)$ quantities. As the companion substrate and thin film chip are cofabricated, these simulations only require slight modification to model the CPW devices with the thin film layer. Since $R(\omega)$ and $L(\omega)$ do not depend strongly on the thin film permittivity, we use the modified FEM simulations to provide the $R(\omega)$ and $L(\omega)$ quantities for the thin film chip. Those values are then used to isolate the quantities $C(\omega)$ and $G(\omega)$ from the thin film measurements. Finally, we sweep the permittivity of the thin film layer in the FEM simulations to obtain the functional relationship between $C(\omega)$ and $G(\omega)$, and the real and imaginary parts of the complex permittivity of the thin film, respectively. Additional description of this calibration, measurement, and analysis protocol can be found in the methods of Ref. [33].

Finally, we measure the voltage tunability of the thin film at 298 K by repeating the complex permittivity measurements, but we use bias tees to combine the ac measurement signal with a dc bias voltage. The dc bias voltage is swept to generate dc electric fields from $-75\,\mathrm{kV cm^{-1}}$ to $+75\,\mathrm{kV cm^{-1}}$ in the gaps of the CPW devices. The dc electric fields induce tuning of the thin film permittivity while we measure the S parameters from 100 MHz to 40 GHz. The frequency range is limited by the bias tees used to apply the dc offset, and we choose the dc field magnitude limit to avoid dielectric breakdown failures in our devices.

III. RESULTS AND DISCUSSION

A. Structural and compositional characterization

The $\Theta - 2\Theta$ XRD patterns of the combinatorial $Ba_{1-x}Sr_xTiO_3$ film clearly illustrate the presence of the composition gradient [Fig. 3(a)]. For the narrow range scans ($2\Theta = 44^\circ$ to $2\Theta = 48^\circ$) shown in Fig. 3(a), the $(002)_{subs}$ peak appears at a consistent position of $2\Theta = 47.0^\circ$ but the $(002)_{film}$ peak shifts from a position of $2\Theta = 45.3^\circ$ on the BTO side of the composition gradient to a position of $2\Theta = 46.1^\circ$ on the STO side. The absence of satellite reflections near the peaks in these scans indicate that we have not made a superlattice of the two constituent materials [35]. Additional scans performed after Au device fabrication that covered a wider range from $2\Theta = 10^\circ$ to $2\Theta = 90^\circ$ reveal only (001), (002), and (003) film and substrate peaks, as well as peaks from the polycrystalline Au conductors, which we interpret as the epitaxial growth of the $Ba_{1-x}Sr_xTiO_3$ combinatorial film on the single crystal (001)-oriented LSAT substrate. Supplemental Φ scans of the (202) film peaks also show four-fold symmetry in the $Ba_{1-x}Sr_xTiO_3$ film and suggest an epitaxial cube-on-cube relationship between the film and the substrate. The composition gradient profiles observed by both WDS and XRD are consistent with each other and show a linear profile between the BTO ($x = 0$) and STO ($x = 1$) regions [Fig. 3(b)].

B. Microwave dielectric spectroscopy

Our measurements of the complex permittivity at room temperature (298 K) from 100 MHz to 110 GHz reveal a large change in the real part of the frequency-dependent dielectric permittivity $[\varepsilon'(\omega)]$ with composition x in $Ba_{1-x}Sr_xTiO_3$ [Fig. 4(a)]. The dielectric permittivity at 110 GHz first increases from 400 for $x = 0$ to a peak

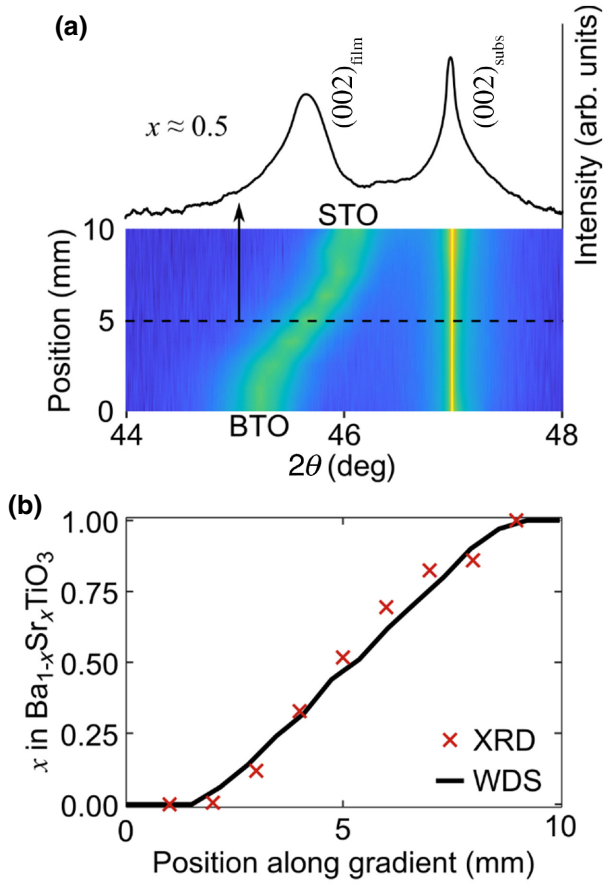

FIG. 3. Structural and compositional characterization provide a picture of the composition profile in the composition-spread thin films. (a) XRD measurements of the composition-spread thin film near the $(002)_{film}$ and $(002)_{subs}$ peaks. The top portion shows a $\Theta - 2\Theta$ scan at the center of the composition gradient ($x \approx 0.5$). The bottom portion is a heatmap of the diffracted intensity in the same 2Θ range across the entire surface of the composition-spread thin film sample, illustrating the shift in the $(002)_{film}$ peak position as the composition changes. (b) Composition profile of the composition-spread thin film as estimated by the application of Vegard's law to the XRD measurements, and as measured by WDS.

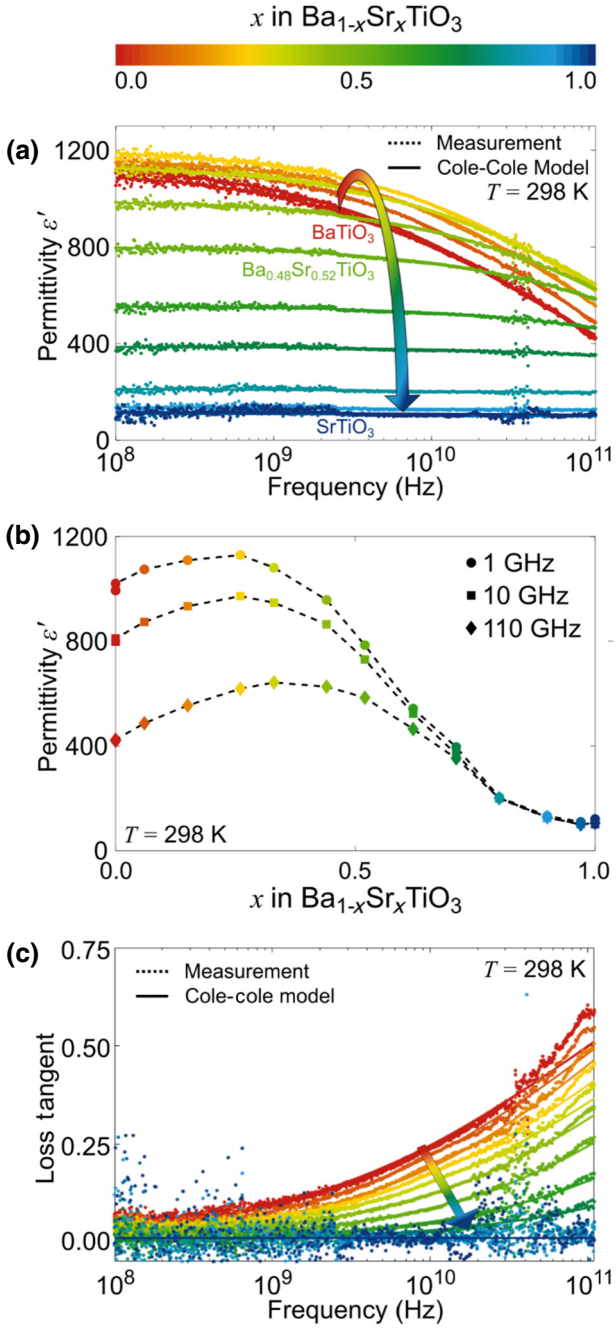

FIG. 4. The room-temperature ($T = 298$ K) dielectric properties of the $Ba_{1-x}Sr_xTiO_3$ composition-spread thin films are highly composition and frequency dependent. (a) The real part of the dielectric permittivity, $\varepsilon'(\omega)$, from 100 MHz to 110 GHz for each of the 14 measured compositions of $Ba_{1-x}Sr_xTiO_3$ from $x = 0$ (red) to $x = 1$ (dark blue) at room temperature. The colored arrow corresponds with the color bar seen at top and indicates the trend in the permittivity as Sr is added, and x in $Ba_{1-x}Sr_xTiO_3$ increases. (b) The room-temperature dielectric permittivity as a function of composition x in $Ba_{1-x}Sr_xTiO_3$ at 1, 10, and 110 GHz. (c) The loss tangent $[\tan\delta = \varepsilon''(\omega)/\varepsilon'(\omega)]$ of the measured compositions x in $Ba_{1-x}Sr_xTiO_3$. The colored arrow again indicates the trend in the loss tangent as x in $Ba_{1-x}Sr_xTiO_3$ increases.

value of 650 for compositions from approximately $x = 0.3$ to $x = 0.4$ and finally decreases to approximately 100 for $x = 1$. The composition-dependent peak in the dielectric permittivity [Fig. 4(b)] is consistent with established reports for thin films of $Ba_{1-x}Sr_xTiO_3$ [19,36,37]. For example, the peak in the permittivity tends to appear near the ferroelectric Curie temperature, T_C, which changes with composition and is near room temperature for compositions of approximately $x = 0.30$ to $x = 0.40$ [19,38,39]. The high permittivity of these compositions at our measurement temperature coincides with a decrease in the soft-mode frequency near T_C [40]. The sudden, strong composition- or temperature-dependent transition often seen in bulk ferroelectric single crystals is not evident

in our measured data. Rather, our thin film $Ba_{1-x}Sr_xTiO_3$ likely undergoes a diffuse phase transition (DPT) due to local strain and size effects [41,42].

The DPT nature of these thin films is also manifest in the broad relaxations with composition-dependent characteristic relaxation times ranging from a few picoseconds to subpicosecond. For compositions where $x > 0.8$, the frequency dependence is effectively negligible. Broad dispersion behavior and other relaxorlike characteristics were previously established in the $Ba_{1-x}Sr_xTiO_3$ system and other DPT ferroelectrics and linked to nanoscale polar regions with a finite distribution of sizes [40]. We explore this composition-dependent relaxation behavior in further detail as part of our discussion of the application of the Cole-Cole model.

The measured loss tangent $[\tan\delta = \varepsilon''(\omega)/\varepsilon'(\omega)]$ of the film also displays a strong composition-dependence [Fig. 4(b)]. The loss tangent across the full frequency range from 100 MHz to 110 GHz decreases monotonically as x increases from $x = 0$ to $x = 1$. The losses for the Ba-rich compositions in our composition-spread $Ba_{1-x}Sr_xTiO_3$ film are large ($\tan\delta > 0.2$) and increase rapidly at millimeter-wave frequencies above 30 GHz. In contrast, when x is close to 1 (Sr-rich), the losses are low ($\tan\delta \approx 0.02$), even at 110 GHz.

C. Voltage tunability measurements

Naturally, measuring the material's response to an applied electric field is important for studying tunable dielectric materials. Figure 5(a) shows the real part of the dielectric permittivity $[\varepsilon'(\omega)]$ with respect to the applied dc electric field from a previously poled state to a maximum applied field of $\pm 75\,\mathrm{kV\,cm^{-1}}$ for five notable compositions x in $Ba_{1-x}Sr_xTiO_3$ at 40 GHz. Here, the total relative tunability (n_r) of the thin film is

$$n_r = \frac{\varepsilon'_{\mathrm{film}}(E_0) - \varepsilon'_{\mathrm{film}}(E_{\mathrm{max}})}{\varepsilon'_{\mathrm{film}}(E_0)}, \tag{2}$$

where $\varepsilon'_{\mathrm{film}}(E_0)$ is the dielectric permittivity of the film without the dc bias field, and $\varepsilon'_{\mathrm{film}}(E_{\mathrm{max}})$ is the permittivity of the film under the maximum dc bias field. The highest observed relative tunability is approximately 50% at our maximum field of $75\,\mathrm{kV\,cm^{-1}}$, but this behavior persists for compositions from $x = 0.0$ to $x = 0.5$ [Fig. 5(b)]. While we expect to see high relative tunability for the compositions with near-room-temperature T_C [43], the broad composition range with high tunability may be explained by the DPT characteristic of these thin films. As we continue to add Sr (i.e., increase x in $Ba_{1-x}Sr_xTiO_3$), both the

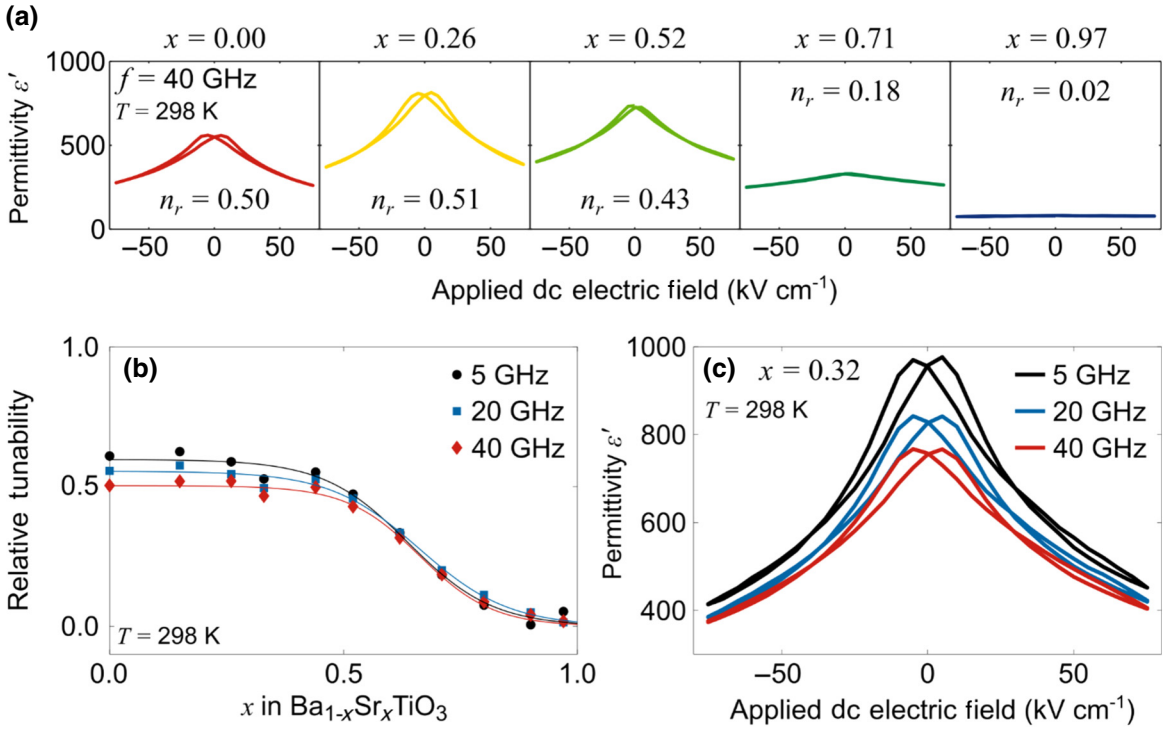

FIG. 5. Applying a dc electric field to the test devices tunes the permittivity of the thin film. (a) The room-temperature ($T = 298$ K) tuning curves of select $Ba_{1-x}Sr_xTiO_3$ compositions at 40 GHz from a previously poled state to a maximum applied field of ± 75 kV cm^{-1}. (b) The room-temperature ($T = 298$ K) relative tunability, n_r, as a function of composition measured at 5, 20, and 40 GHz. (c) The room-temperature ($T = 298$ K) tuning curves for the $x = 0.68$ thin film composition at 5, 20, and 40 GHz.

relative tunability [Fig. 5(b)] and the hysteresis [Fig. 5(a)] in the tuning curves decrease. The reduction in hysteresis is expected for these Sr-rich compositions that are deeper in the paraelectric state. The more tunable Ba-rich compositions also exhibit frequency dependence of the tunability [Figs. 5(b) and 5(c)]. For example, the general shape of the tuning curves for the $x = 0.32$ composition is comparable across frequencies [Fig. 5(c)], but the overall tunability is about 10% less at 40 GHz than it is at 5 GHz. As we noted, there is an intimate relationship between the electric-field dependent dielectric behavior of these materials and the distance between the measurement temperature and the T_C of the material under test.

D. Application of the Cole-Cole model

We apply the Cole-Cole model to our dielectric measurement results [44,45]. The Cole-Cole model is a modification of the simpler Debye model, and accommodates a distribution of relaxation times, which can be necessary for DPT ferroelectrics. Such a distribution of relaxation times may arise from a distribution of sizes of the defect-induced nanopolar regions within our film [40,46]. Our selection of the Cole-Cole model is in part due to the prevalence of this model in reports on similar materials in the literature (i.e., thin films of $Ba_{1-x}Sr_xTiO_3$ on crystalline substrates), and due to our measurement bandwidth [14,46,47]. We note that while our measurements reach higher frequencies than most comparable reports, we do not capture the descending slope of the peak in the dielectric loss. Such measurements are key in applying the technique proposed by Jonscher [48,49] to determine whether Cole-Davidson [50] or Havriliak-Negami [51] models are more accurate models at high frequency. The broadness of the relaxations we observe in our measurements, and the parameters obtained preclude our use of the Cole-Davidson model.

We simultaneously fit the real and imaginary parts of the complex permittivity $\varepsilon^*(\omega)$ for each composition x in $Ba_{1-x}Sr_xTiO_3$ with $x < 0.8$ to the Cole-Cole model

$$\varepsilon^*(\omega) = \varepsilon_\infty + \frac{\varepsilon_s - \varepsilon_\infty}{1 + (i\omega\tau)^\beta}\ , \tag{3}$$

where ε_s is the static dielectric permittivity, ε_∞ is the "infinite frequency" permittivity, τ is a generalized relaxation time, and β is a parameter describing the width of the distribution of relaxation times. With the focus of this work being high-frequency dielectric behavior, and the fact that our measurements do not extend below 100 MHz, we do not include an additional parameter for the static electrical conductivity in the modeling used in this work. We do not apply the Cole-Cole model to compositions with $x > 0.8$ because these compositions display virtually no frequency dependence of the dielectric permittivity. That is to say that the relaxations in these compositions occur outside our measurable frequency range. For these compositions, we simply provide the value ε_s as a constant value for the real part of the complex permittivity, and note that the measured loss tangent for these compositions is near or below the detectable limit for typical transmission line measurements of approximately 1% [28]. We determine the fit parameters through nonlinear least squares fitting and simultaneously provide the measurement frequencies, the real part of the measured relative permittivity, and the imaginary part of the measured relative permittivity so that the fitting algorithm can converge with input from these important factors. The best-fit parameters are provided in Table I along with uncertainties representing the 95% confidence interval derived from the calculated residuals during fitting. Fixing some modeled parameters to known values can improve modeling results. The infinite-frequency dielectric permittivity, ε_∞, is given a fixed value of 5.8 based on measurements of the index of refraction of similar materials at optical frequencies [52,53]. The static dielectric permittivity, ε_s, is allowed to vary because a constant value for this parameter is not apparent at 100 MHz for many of the measured compositions. That is to say, the permittivity is still changing at our lower-bound measurement frequency. All other parameters are free to vary within reasonable bounds. The Cole-Cole fits are also included as the solid lines shown in Figs. 4(a) and 4(c). While most of the models fit the data exceptionally well, there are some small but noticeable differences in the loss tangent curves for the most Ba-rich compositions above 60 GHz. This additional loss may be due to a secondary loss mechanism in the material, radiation in the devices, or some as-yet-unaccounted-for error in the metrology. The ongoing development of on-wafer measurements to 220 GHz will further explore this behavior.

TABLE I. Cole-Cole model parameters and relative tunability of $Ba_{1-x}Sr_xTiO_3$

x	ε_s	τ (ps)	β	n_r
0.00	1122 ± 3.97	3.317 ± 0.463	0.50 ± 0.02	0.50
0.00	1157 ± 3.86	3.524 ± 0.401	0.49 ± 0.02	—
0.06	1170 ± 1.97	2.514 ± 0.254	0.51 ± 0.01	—
0.15	1177 ± 1.45	1.750 ± 0.137	0.53 ± 0.01	0.51
0.26	1212 ± 1.58	1.396 ± 0.097	0.51 ± 0.01	0.51
0.32	1147 ± 1.50	1.007 ± 0.062	0.50 ± 0.00	0.47
0.44	995 ± 1.33	0.643 ± 0.036	0.51 ± 0.00	0.50
0.52	803 ± 1.25	0.324 ± 0.019	0.53 ± 0.00	0.43
0.62	555 ± 1.14	0.115 ± 0.008	0.53 ± 0.01	0.31
0.71	388 ± 1.25	0.030 ± 0.005	0.50 ± 0.03	0.18
0.80	225 ± 15	—	—	0.07
0.90	122 ± 13	—	—	0.03
0.97	88 ± 12	—	—	0.02
1.00	84 ± 20	—	—	—

ε_∞ is given a fixed value of 5.8, the approximate permittivity at optical frequencies.

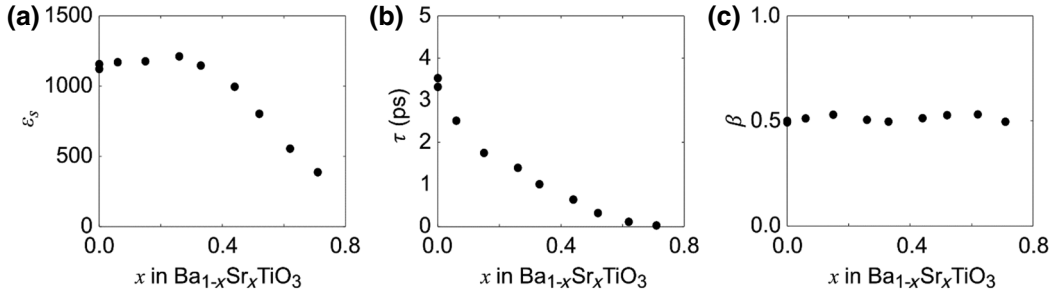

FIG. 6. The composition-dependent Cole-Cole fit parameters provide a means to determine the dielectric properties of these $Ba_{1-x}Sr_xTiO_3$ thin films at specific frequencies and compositions. These parameters are (a) the static-limit permittivity, ε_s, (b) the characteristic relaxation time τ, and (c) the parameter β, which describes the width of the distribution of relaxation times. In all panels, black points represent the parameters of the Cole-Cole fits to the complex permittivity for each of our measured compositions.

The Cole-Cole fit parameters are strongly composition dependent (Fig. 6). The static-limit permittivity, ε_s, is large for the Ba-rich compositions ($x < 0.5$) and mirrors the composition-dependent trend illustrated by Fig. 4(b). The critical relaxation time τ decreases monotonically as Sr is added, or put another way, as x in $Ba_{1-x}Sr_xTiO_3$ increases. This dependence indicates that the relaxation moves from frequencies in the hundreds of gigahertz to frequencies above 1 THz as x decreases. In the past, similar behavior was linked to changes in the distribution of polar nanoregions [40]. As we previously noted, for compositions of x in $Ba_{1-x}Sr_xTiO_3$ above $x = 0.8$, there is very little dispersion in the permittivity, which is consistent with previous studies [19]. More sensitive measurements or measurements to higher frequencies are likely to be needed to reveal additional details of the dispersion behavior for these Sr-rich compositions, especially measurements near the soft-mode phonon frequencies expected between 2 and 3 THz [54]. Finally, the fit parameter representing the width of the distribution of relaxation times, β, is approximately 0.5 for all measured compositions from $x = 0.0$ to $x = 0.8$, deviating from the Debye-like value of $\beta = 1$.

IV. CONCLUSIONS

In conclusion, we develop a technique for extracting the complex permittivity and relative tunability of composition-spread thin films from 100 MHz to 110 GHz. To demonstrate our technique, we explore PLD-grown composition-spread $Ba_{1-x}Sr_xTiO_3$ thin films. Our investigation reveals how the frequency- and voltage-dependent dielectric properties of $Ba_{1-x}Sr_xTiO_3$ change with composition, while holding all other measurement, processing, and growth variables constant. While many individual $Ba_{1-x}Sr_xTiO_3$ compounds have been described elsewhere in the literature, this report is a comprehensive study of the complete $Ba_{1-x}Sr_xTiO_3$ system for application to next-generation telecommunications, providing models for key properties as a function of frequency, voltage, and composition. Since T_C changes with composition in the $Ba_{1-x}Sr_xTiO_3$ system, our composition-dependent measurements provide a window into the diffuse pretransitional effects that can exist above T_C in ferroelectric thin films. Temperature-dependent measurements would provide an additional axis through which we can make an even more comprehensive study of these effects. Future experiments will include characterization of similar samples on a probe station with heating and cryogenic capabilities to fully explore the temperature-dependence of the dielectric properties.

To summarize, we combine the highly controlled growth and processing inherent to combinatorial synthesis with broadband, quantitative, on-wafer permittivity measurements. Our measurements and models provide fresh insight into the tunability and dispersion characteristics of $Ba_{1-x}Sr_xTiO_3$ for many combinations of composition and frequency that have not yet been presented in the literature, yet are highly pertinent to applied industrial physicists working with tunable materials. We envision this insight presenting theorists with the comprehensive data needed to build more robust models of dielectric loss and tunability, giving materials scientists a more complete understanding of how this materials system behaves at high frequencies and a target for further improvement, and providing engineers with key property measurements relevant to device performance in systems like beam-forming antennas and tunable filters. Going forward, we hope to incorporate our results with mesoscale modeling to better understand how polar nanoregions and local ordering affect relaxation behavior and apply this technique to study multiferroic systems such as $Bi_{1-x}Sm_xFeO_3$. Like many other fresh insights into applied physics and materials science, we raise as many questions as we answer. How does this relaxation change across the landscape of temperature, field, and composition? These and other questions will further our understanding of the relationships between structure, loss, and tunability in commercially relevant tunable dielectrics for 5G and other uses. The comprehensive data that can be quickly obtained by our technique provides an ideal platform to study entire material systems and better

inform computational models that play an increasing role in high-frequency materials discovery and understanding the materials genome.

Data from this article is available from the authors upon reasonable request.

ACKNOWLEDGMENTS

The authors thank Dr. Angela Stelson, Dr. Kassi Smith, and Dr. Nina Popovic of the National Institute of Standards and Technology (NIST), for their critical feedback during this research. The authors also thank Dr. Yangang Liang formerly with the University of Maryland for helpful discussion regarding the combinatorial thin film deposition.

Contributions to this article by workers at NIST, an agency of the U.S. Government, are not subject to U.S. copyright.

[1] S. Mahon, The 5G effect on RF filter technologies, IEEE Trans. Semicond. Manuf. **30**, 494 (2017).

[2] C. Schuster, A. Wiens, F. Schmidt, M. Nickel, M. Schubler, R. Jakoby, and H. Maune, Performance analysis of reconfigurable bandpass filters With continuously tunable center frequency and bandwidth, IEEE Trans. Microwave Theory Tech. **65**, 4572 (2017).

[3] G. Subramanyam, M. W. Cole, N. X. Sun, T. S. Kalkur, N. M. Sbrockey, G. S. Tompa, X. Guo, C. Chen, S. P. Alpay, G. A. Rossetti, K. Dayal, L.-Q. Chen, and D. G. Schlom, Challenges and opportunities for multi-functional oxide thin films for voltage tunable radio frequency/microwave components, J. Appl. Phys. **114**, 191301 (2013).

[4] A. K. Tagantsev, V. O. Sherman, K. F. Astafiev, J. Venkatesh, and N. Setter, Ferroelectric materials for microwave tunable applications, J. Electroceram. **11**, 5 (2003).

[5] S. Gevorgian, *Ferroelectrics in Microwave Devices, Circuits and Systems: Physics, Modeling, Fabrication and Measurements* (Springer Science & Business Media, London, 2009).

[6] T. S. Kalkur, N. Sbrockey, G. S. Tompa, and M. W. Cole, Tunable RF filters fabricated using MOCVD deposited graded composition BST films, Integr. Ferroelectr. **126**, 28 (2011).

[7] R. De Paolis, S. Payan, M. Maglione, G. Guegan, and F. Coccetti, High-Tunability and high Q-factor integrated ferroelectric circuits up to millimeter waves, IEEE Trans. Microwave Theory Tech. **63**, 2570 (2015).

[8] H. Jiang, M. Patterson, D. Brown, C. Zhang, K. Pan, G. Subramanyam, D. Kuhl, K. Leedy, and C. Cerny, Miniaturized and reconfigurable CPW square-ring slot antenna loaded With ferroelectric BST thin film varactors, IEEE Trans. Antennas Propag. **60**, 3111 (2012).

[9] M. T. Sebastian, R. Ubic, and H. Jantunen, *Microwave Materials and Applications* (John Wiley & Sons, Hoboken, NJ, 2017).

[10] S. S. Gevorgian and E. L. Kollberg, Do we really need ferroelectrics in paraelectric phase only in electrically controlled microwave devices?, IEEE Trans. Microwave Theory Tech. **49**, 2117 (2001).

[11] Z. Gu, et al., Resonant domain-wall-enhanced tunable microwave ferroelectrics, Nature **560**, 622 (2018).

[12] M. W. Cole, R. C. Toonen, M. Ivill, S. G. Hirsch, E. Ngo, and C. Hubbard, Ultraviolet assisted processing: A unique approach to mitigate oxygen vacancies and attain low loss highly tunable $Ba_{0.60}Sr_{0.40}TiO_3$ thin films, J. Appl. Phys. **110**, 124105 (2011).

[13] T. J. Jackson and I. P. Jones, Nanoscale defects and microwave properties of $(Ba, Sr)TiO_3$ ferroelectric thin films, J. Mater. Sci. **44**, 5288 (2009).

[14] J. C. Booth, I. Takeuchi, and K.-S. Chang, Microwave-frequency loss and dispersion in ferroelectric $Ba_{0.3}Sr_{0.7}TiO_3$ thin films, Appl. Phys. Lett. **87**, 082908 (2005).

[15] C. J. G. Meyers, C. R. Freeze, S. Stemmer, and R. A. York, $(Ba, Sr)TiO_3$ tunable capacitors with RF commutation quality factors exceeding 6000, Appl. Phys. Lett. **109**, 112902 (2016).

[16] C.-H. Lee, et al., Exploiting dimensionality and defect mitigation to create tunable microwave dielectrics, Nature **502**, 532 (2013).

[17] B. G. Sumpter, R. K. Vasudevan, T. Potok, and S. V. Kalinin, A bridge for accelerating materials by design, npj Comput. Mater. **1**, 15008 (2015).

[18] X. D. Xiang, X. Sun, G. Briceno, Y. Lou, K. A. Wang, H. Chang, W. G. Wallace-Freedman, S. W. Chen, and P. G. Schultz, A combinatorial approach to materials discovery, Science **268**, 1733 (1995).

[19] K. S. Chang, M. Aronova, O. Famodu, I. Takeuchi, S. E. Lofland, J. Hattrick-Simpers, and H. Chang, Multimode quantitative scanning microwave microscopy of in situ grown epitaxial $Ba_{1-x}Sr_xTiO_3$ composition spreads, Appl. Phys. Lett. **79**, 4411 (2001).

[20] D. J. Barker, P. M. Suherman, T. J. Jackson, and M. J. Lancaster, *18th IEEE ISAF* (IEEE, Xian, CN, 2009), pp. 1–6.

[21] D. J. Barker, T. J. Jackson, P. M. Suherman, M. S. Gashinova, and M. J. Lancaster, Uncertainties in the permittivity of thin films extracted from measurements with near field microwave microscopy calibrated by an image charge model, Meas. Sci. Tech. **25**, 105601 (2014).

[22] B.-Y. Wu, X.-Q. Sheng, R. Fabregas, and Y. Hao, Full-wave modeling of broadband near field scanning microwave microscopy, Sci. Rep. **7**, 16064 (2017).

[23] K. R. Talley, S. L. Millican, J. Mangum, S. Siol, C. B. Musgrave, B. Gorman, A. M. Holder, A. Zakutayev, and G. L. Brennecka, Implications of heterostructural alloying for enhanced piezoelectric performance of (Al, Sc)N, Phys. Rev. Mater. **2**, 063802 (2018).

[24] G. Koren and E. Polturak, Is $LaAlO_3$ a viable substrate for the deposition of high quality thin films of $YBa_2Cu_3O_{7-\delta}$, Supercond. Sci. Technol. **15**, 1335 (2002).

[25] L. Vegard, Die konstitution der mischkristalle und die raumfüllung der atome, Z. Phys. **5**, 17 (1921).

[26] M. Zhengxiang, A. J. Becker, P. Polakos, H. Huggins, J. Pastalan, W. Hui, K. Watts, Y. H. Wong, and P. Mankiewich, RF measurement technique for characterizing

thin dielectric films, IEEE Trans. Electron Devices **45**, 1811 (1998).

[27] P. Rundqvist, A. Vorobiev, S. Gevorgian, and K. Khamchane, Non-Destructive microwave characterization of ferroelectric films on conductive substrates, Integr. Ferroelectr. **60**, 1 (2004).

[28] J. Baker-Jarvis, M. D. Janezic, and D. C. DeGroot, High-frequency dielectric measurements, IEEE Trans. Instrum. Meas. **13**, 24 (2010).

[29] R. B. Marks, A multiline method of network analyzer calibration, IEEE Trans. Microwave Theory Tech. **39**, 1205 (1991).

[30] R. N. Simons, *Coplanar Waveguide Circuits, Components, and Systems* (Wiley Online Library, Hoboken, NJ, 2001).

[31] N. D. Orloff, J. Mateu, A. Lewandowski, E. Rocas, J. King, D. Gu, X. Lu, C. Collado, I. Takeuchi, and J. C. Booth, A compact variable-temperature broadband series-resistor calibration, IEEE Trans. Microwave Theory Tech. **59**, 188 (2011).

[32] D.F. Williams, C.M. Wang, U. Arz, in *IEEE MTT-S International Microwave Symposium Digest*, edited by Herb Thal and Paul Eitner (IEEE, Philadelphia, PA, 2003), pp. 1819–1822.

[33] N. M. Dawley, E. J. Marksz, A. M. Hagerstrom, G. H. Olsen, M. E. Holtz, V. Goian, C. Kadlec, J. Zhang, X. Lu, J. A. Drisko, R. Uecker, S. Ganschow, C. J. Long, J. C. Booth, S. Kamba, C. J. Fennie, D. A. Muller, N. D. Orloff, and D. G. Schlom, Targeted chemical pressure yields tuneable millimetre-wave dielectric, Nat. Mater. **19**, 176 (2020).

[34] H. Ulrich, R. W. Wijnaendts-Van-Resandt, C. Rensch, and W. Ehrensperger, Direct writing laser lithography for production of microstructures, Microelectron. Eng. **6**, 77 (1987).

[35] A. Authier, S. Lagomarsino, and B. K. Tanner, *X-ray and Neutron Dynamical Diffraction: Theory and Applications* (Springer Science & Business Media, New York, NY, 2012).

[36] S. U. Adikary and H. L. W. Chan, Ferroelectric and dielectric properties of sol–gel derived $Ba_xSr_{1-x}TiO_3$ thin films, Thin Solid Films **424**, 70 (2003).

[37] Y. Gim, T. Hudson, Y. Fan, C. Kwon, A. T. Findikoglu, B. J. Gibbons, B. H. Park, and Q. X. Jia, Microstructure and dielectric properties of $Ba_{1-x}Sr_xTiO_3$ films grown on $LaAlO_3$ substrates, Appl. Phys. Lett. **77**, 1200 (2000).

[38] B. H. Hoerman, G. M. Ford, L. D. Kaufmann, and B. W. Wessels, Dielectric properties of epitaxial $BaTiO_3$ thin films, Appl. Phys. Lett. **73**, 2248 (1998).

[39] R. C. Pullar, Y. Zhang, L. Chen, S. Yang, J. R. G. Evans, P. K. Petrov, A. N. Salak, D. A. Kiselev, A. L. Kholkin, V. M. Ferreira, and N. M. Alford, Manufacture and measurement of combinatorial libraries of dielectric ceramics: Part II. dielectric measurements of $Ba_{1-x}Sr_xTiO_3$ libraries, J. Eur. Ceram. Soc. **27**, 4437 (2007).

[40] T. Teranishi, T. Hoshina, H. Takeda, and T. Tsurumi, Polarization behavior in diffuse phase transition of $Ba_xSr_{1-x}TiO_3$ ceramics, J. Appl. Phys. **105**, 054111 (2009).

[41] S. Chattopadhyay, P. Ayyub, V. R. Palkar, and M. Multani, Size-induced diffuse phase transition in the nanocrystalline ferroelectric $PbTiO_3$, Phys. Rev. B Condens. Matter **52**, 13177 (1995).

[42] T. M. Shaw, Z. Suo, M. Huang, E. Liniger, R. B. Laibowitz, and J. D. Baniecki, The effect of stress on the dielectric properties of barium strontium titanate thin films, Appl. Phys. Lett. **75**, 2129 (1999).

[43] M. Jain, E. Bauer, Y. Lin, H. Wang, A. Burrell, T. McClesky, and Q. Jia, BaTiO3-related ferroelectric thin films by polymer assisted deposition, Integr. Ferroelectr. **100**, 132 (2010).

[44] K. S. Cole and R. H. Cole, Dispersion and absorption in dielectrics II. Direct current characteristics, J. Chem. Phys. **10**, 98 (1942).

[45] R. H. Cole and K. S. Cole, Dispersion and absorption in dielectrics I. Alternating current characteristics, J. Chem. Phys. **9**, 341 (1941).

[46] G. Houzet, K. Blary, S. Lepilliet, D. Lippens, L. Burgnies, G. Vélu, J.-C. Carru, E. Nguéma, and P. Mounaix, Dielectric dispersion of $BaSrTiO_3$ thin film from centimeter to submillimeter wavelengths, J. Appl. Phys. **109**, 014116 (2011).

[47] G. Houzet, L. Burgnies, G. Velu, J.-C. Carru, and D. Lippens, Dispersion and loss of ferroelectric $Ba_{0.5}Sr_{0.5}TiO_3$ thin films up to 110GHz, Appl. Phys. Lett. **93**, 053507 (2008).

[48] A. K. Jonscher, Physical basis of dielectric loss, Nature **253**, 717 (1975).

[49] C. L. Wang, Jonscher indices for dielectric materials, J. Adv. Dielectrics **09**, 1950046 (2019).

[50] D. W. Davidson and R. H. Cole, Dielectric relaxation in glycerol, propylene glycol, and n-propanol, J. Chem. Phys. **19**, 1484 (1951).

[51] S. Havriliak and S. Negami, A complex plane representation of dielectric and mechanical relaxation processes in some polymers, Polymer **8**, 161 (1967).

[52] M. J. Weber, *Handbook of Laser Science and Technology: Properties. Optical Materials, P. 2* (CRC, Boca Raton, FL, 1986).

[53] S. H. Wemple, M. Didomenico, and I. Camlibel, Dielectric and optical properties of melt-grown BaTiO3, J. Phys. Chem. Solids **29**, 1797 (1968).

[54] J. Weerasinghe, L. Bellaiche, T. Ostapchuk, P. Kužel, C. Kadlec, S. Lisenkov, I. Ponomareva, and J. Hlinka, Emergence of central mode in the paraelectric phase of ferroelectric perovskites, MRS Commun. **3**, 41 (2013).